Vegetation optical depth and scattering albedo retrieval using time series of dual-polarized L-band radiometer observations

CrossMark

Alexandra G. Konings [a],[*],[1], María Piles [b],[1], Kathrina Rötzer [c], Kaighin A. McColl [a], Steven K. Chan [d], Dara Entekhabi [a]

[a] Department of Civil and Environmental Engineering, Massachusetts Institute of Technology, Cambridge, MA 02139, USA
[b] Departament de Teoria del Senyal i Comunicacions, Universitat Politècnica de Catalunya (UPC), IEEC/UPC and SMOS Barcelona Expert Center (SMOS-BEC), 08034 Barcelona, Spain
[c] Agrosphere Institute, Forschungszentrum Jülich, 52428 Jülich, Germany
[d] Jet Propulsion Laboratory, California Institute of Technology, Pasadena, CA 91109, USA

ABSTRACT

Passive microwave measurements have the potential to estimate vegetation optical depth (VOD), an indicator of aboveground vegetation water content. They are also sensitive to the vegetation scattering albedo and soil moisture. In this work, we propose a novel algorithm to retrieve VOD and soil moisture from time series of dual-polarized L-band radiometric observations along with time-invariant scattering albedo. The method takes advantage of the relatively slow temporal dynamics of early morning vegetation water content and combines a number of consecutive observations to estimate a single VOD. It is termed the multi-temporal dual channel algorithm (MT-DCA). The soil dielectric constant (directly related to soil moisture) of each observation is also retrieved simultaneously. Additionally, the method retrieves a constant albedo, thereby providing for the first time information on global single-scattering albedo variations. The algorithm is tested using three years of L-band passive observations from the NASA Aquarius sensor. The global VOD distribution follows expected gradients of climate and canopy biomass conditions. Its seasonal dynamics follow expected behavior based on precipitation and land cover. The retrieved VOD is closely related to coincident cross-polarized backscatter coefficients. The VOD and dielectric retrievals from MT-DCA are compared to those obtained from implementing the commonly used Land Parameter Retrieval Model (LPRM) algorithm and shown to have less high-frequency noise. There is almost as much variation in MT-DCA retrieved albedo between pixels of a given land cover class than between land cover classes, suggesting the common approach of assigning albedo based on land cover class may not capture its spatial variability. Globally, albedo appears to be primarily sensitive to woody biomass. The proposed algorithm allows for a more accurate accounting of the effects of vegetation on radiometric soil moisture retrievals, and generates new observations of L-band VOD and effective single-scattering albedo. These new datasets are complementary to existing remotely sensed vegetation measurements such as fluorescence and optical-infrared indices.

© 2015 Elsevier Inc. All rights reserved.

1. Introduction

Our ability to close the Earth's carbon budget and predict feedbacks in a changing climate depends on knowing where, when and how much carbon dioxide and water vapor is exchanged between the land surface and the atmosphere. Both these fluxes are intimately tied to vegetation: roughly 60% of global land evapotranspiration fluxes occur through plant-mediated transpiration (Schlesinger & Jasechko, 2014), and vegetation photosynthesis response to increasing CO_2 concentrations is the biggest carbon cycle feedback in climate models (Ciais et al., 2013; Schimel, Stephens, & Fisher, 2014). Microwave radiometric data at L-band are sensitive to both vegetation characteristics and soil moisture. In particular, radiometric observations are sensitive to vegetation optical depth (VOD). Passive soil moisture retrieving satellites at L-band like the NASA Soil Moisture Active Passive (SMAP) (Entekhabi et al., 2010), the ESA Soil Moisture and Ocean Salinity (SMOS) (Kerr et al., 2012), and the NASA/CONAE Aquarius-SAC-D (Le Vine, Lagerloef, Colomb, Yueh, & Pellerano, 2007) must properly account for the effect of VOD on observations in order to accurately retrieve soil moisture. Furthermore, microwave VOD estimates have previously been shown to be useful indicators for understanding vegetation state and variability, complementing the information provided by optical indices (Andela, Liu, van Dijk, de Jeu, & McVicar, 2013; Poulter et al., 2014; Zhou et al., 2014). VOD is also a potentially

---

[*] Corresponding author.
[1] Equally contributing authors.

useful tool for crop monitoring (Patton & Hornbuckle, 2013) that could help detect crop water stress before optical sensors can (Van Emmerik, Steele-Dunne, Judge, & van de Giesen, 2014). VOD is directly proportional to total vegetation water content (VWC), with a constant of proportionality that is dependent on frequency and canopy structure. Since total VWC is related to biomass (it influences the amount of available storage for water), VOD has been used as an indicator of biomass in the past (e.g. Liu et al., 2015). However, since vegetation water content also varies depending on the soil water availability (even in the absence of changes in biomass), VOD can also be interpreted as an indicator of vegetation water content useful for studying plant responses to hydrologic stress.

The VOD measured by passive microwave sensors is an integrated measure of vegetation water content and structural effects. The total VOD is always less sensitive to the lower canopy layers than to the upper canopy layers, although the exact rate of attenuation of the microwave signal depends on the canopy. The rate of attenuation is also frequency-dependent (Ulaby, Moore, & Fung, 1986), although few studies have been done comparing the effect of frequency on the measured VOD. If differences in canopy penetration between observations at different frequencies are ignored, different satellites can be combined into a single long-term record of VOD (Owe, de Jeu, & Holmes, 2008; Liu, de Jeu, McCabe, Evans, & van Dijk, 2011). Such an existing record has been used as a vegetation indicator complementary to optical indices (Shi et al., 2008; Andela et al., 2013). VOD retrievals from recently launched L-band radiometers such as SMOS and SMAP could be used to extend long-term multi-frequency VOD records (Van der Schalie, Parinussa, et al., 2015). Additionally, vegetation water content, and thus the amount of plant stress inferred by measuring vegetation water content, generally varies throughout the canopy (e.g., Hellkvist, Richards, & Jarvis, 1974; Bohrer et al., 2005; Janott et al., 2011). Studies of vegetation water content based on remote sensing may thus be better served by using VOD from lower frequencies such as L-band, which attenuate less quickly and are more sensitive to lower canopy layers. Furthermore, the development of VOD datasets and of joint VOD and soil moisture retrieval algorithms at L-band is of interest because of the greater soil sensing depth of these frequencies.

Several approaches exist for the simultaneous retrieval of vegetation optical depth and soil moisture that is necessary at L-band. Both variables can be simultaneously derived from a snapshot of measurements by using information from observations at both horizontal and vertical polarizations (Jackson, Hsu, & O'Neill, 2002; Meesters, de Jeu, & Owe, 2005). However, because the two polarizations are closely correlated, such a retrieval is sensitive to noise, as will be further explained in Section 2. If multi-angular data are available, such as in the case of SMOS, these can be used to further constrain the retrievals (Cui, Shi, Du, Zhao, & Xiong, 2015). Alternatively, observations from multiple overpasses can be combined into a single retrieval. Such a multi-temporal approach rests on the assumption that vegetation state as reflected in VOD is likely to change more slowly than soil moisture, and is constant over adjacent overpasses.

The use of a time series approach also allows for the retrieval of the single-scattering albedo, the amount of power scattered by the vegetation cover. The value of albedo is often assumed to be independent of polarization and constant as a function of land cover (Van de Griend & Owe, 1994; O'Neill, Chan, Njoku, Jackson, & Bindlish, 2012; Kerr et al., 2011). Its values are often close to zero (Wigneron et al., 2004). A correctly chosen effective value of the single-scattering albedo allows accounting for higher-order scattering effects, which are especially important over moderate to dense vegetation cover (Kurum et al., 2012). Many of the land-cover dependent values used in the literature are therefore in some sense fitting-parameters (Wigneron et al., 2004; Kurum, 2013). However, a land-cover dependent assignment is sensitive to errors in the land cover classifications, as well as to variations in albedo within a certain land cover type. A sensitivity study has shown that errors in assumed albedo add more uncertainty to single-

incidence angle VOD and soil moisture retrievals than errors in soil and canopy temperature, soil roughness, or bias or noise in observed brightness temperature (Davenport, Fernandez-Galvez, & Gurney, 2005). The ability to retrieve albedo directly rather than relying on assumptions about its value may therefore significantly improve both VOD and soil moisture retrievals.

In this study, we introduce a new multi-temporal algorithm for simultaneous retrieval of vegetation optical depth, effective single-scattering albedo, and soil dielectric constant using dual-polarized single incidence-angle observations at L-band frequencies. The method is referred to as the multi-temporal dual channel algorithm (MT-DCA) and tested using three years of L-band passive observations from the Aquarius sensor. The paper is organized as follows. Section 2 motivates the need for a time series algorithm to avoid compensating errors when retrieving multiple parameters from a snapshot of dual-polarized observations. Section 3 describes the algorithm design. The testing methodology and datasets used in this paper are described in Sections 4 and 5, respectively. Retrieval results are shown in Section 6 and discussed in Section 7.

2. Algorithm motivation

2.1. Classical retrieval approach

Almost all radiometric soil moisture retrieval approaches are based on the so-called τ–ω model, a zeroth-order solution of the radiative transfer equations describing the emission of the land surface

$$
\begin{aligned}
T_{B_p} &= T_B^{soil} + T_B^{canopy} \\
&= T_s(1-r_p)\gamma + T_c(1-\omega)(1-\gamma)(1+r_p\gamma).
\end{aligned}
\tag{1}
$$

The T_{B_p} is the brightness temperature at polarization p, which is either horizontal (H) or vertical (V), T_s is the effective land surface temperature, r_p is the rough surface reflectivity, and T_c is the canopy temperature. The quantity γ is the vegetation transmissivity and ω is the vegetation single-scattering albedo, the fractional power scattered by the vegetation.

The vegetation transmissivity γ accounts for attenuation of the emission through the vegetation layer. It is related to the vegetation optical depth,

$$
\gamma = \exp\left(-\frac{\text{VOD}}{\cos\theta}\right),
\tag{2}
$$

where θ is the measurement incidence angle. When the VOD equals 0, there is no vegetation attenuation on the microwave emission from the soil and the corresponding γ is 1. The VOD increases with vegetation density; over dense vegetation, γ approaches 0 and the microwave emission is dominated by vegetation. VOD is commonly assumed to be linearly proportional to vegetation water content (Jackson & Schmugge, 1991; Van De Griend & Wigneron, 2004),

$$
\text{VOD} = b \cdot \text{VWC},
\tag{3}
$$

where the constant of proportionality b depends on the vegetation structure.

The rough surface reflectivity can be decomposed as $r_p = r_p^* \exp(-h\cos(\theta)^n)$, where r_p^* is the reflectivity of the flat (smooth) soil, h is the roughness parameter, which is assumed to be linearly related to the root-mean-square surface height of the soil surface, and n is an angular value (Ulaby & Long, 2014). The Fresnel equations relate r_p^* to the complex dielectric constant k of the soils, which is in turn governed by soil moisture and soil texture.

Most soil moisture retrieval algorithms rely on the same (or an equivalent) mathematical problem. In order to determine the vector of unknown parameters X from a set of observations, the mismatch

between the observed ($T_{B_p}{}^{obs}$) and modeled brightness temperatures ($T_{B_p}{}^{model}(X)$) is minimized,

$$X = \min_X \; J = \sum_{p=H,V} \left(T_{B_p}^{obs} - T_{B_p}^{model}(X) \right)^2, \qquad (4)$$

where p represents the polarization.

There are a variety of algorithms that differ in how many observations are combined – whether the sum over polarization is included or whether additional summations are made over different incidence angles, frequencies, or overpasses – and in how many unknowns are included in X. The cost function in Eq. (4) can also incorporate additional terms to account for a priori information on the unknown parameters and its associated uncertainty (Piles, Vall-llossera, Camps, Talone, & Monerris, 2010), which is the solution adopted for the SMOS L2 processor (Kerr et al., 2011). Soil moisture is a key unknown and is always retrieved. By contrast, additional parameters such as h, ω, and VOD can be either assigned dependent on some ancillary information or retrieved alongside soil moisture.

2.2. Time series motivation

In order for the retrieved values to be stable – that is, insensitive to measurement noise – the algorithm cannot have more unknowns than the degrees of freedom provided by the measurements considered. If this requirement is not met, the global minimum of the cost function in Eq. (4) will be overly sensitive to measurement noise or small imperfections in the radiative transfer model. For the SMOS satellite, multiple incidence angles are used to obtain additional degrees of freedom (Kerr et al., 2012). For data where only a single frequency and incidence angle is available, either a so-called single-channel algorithm using a single polarization (e.g. Bindlish, Jackson, Cosh, Zhao, & O'Neill, 2015) or a dual-channel algorithm (DCA) using both the horizontal and vertical polarizations (e.g. Jackson et al., 2002) can be used. A commonly used variant of the traditional dual channel algorithm is the Land Parameter Retrieval Model or LPRM (Owe et al., 2008). It uses only the H-polarization in the cost function, but also uses the V-polarization as an additional piece of information by algebraically re-arranging the tau–omega model to provide a direct relationship between k and VOD (Meesters et al., 2005) that is a function of the multi-polarization difference index (Owe, de Jeu, & Walker, 2001). For both the traditional DCA and LPRM, two polarizations are used to retrieve two unknowns.

Because the horizontally and vertically polarized brightness temperatures are highly correlated, there is duplicate information in the two measurements. This duplicate information reduces the ability of a DCA or similar algorithms to robustly retrieve two parameters in the presence of measurement or modeling noise and adds errors to the retrievals (Konings, McColl, Piles, & Entekhabi, 2015). This is illustrated in Fig. 1. The background colors show the cost function, as a function of VOD and k, for a sample set of observations. The perfect retrievals would be those leading to the minimum of the cost function, indicated by a black dot. Small amounts of noise ($\Delta e_H = 0.005$, $\Delta e_v = -0.002$) are added to the 'observed emissivities' to simulate observational or model noise. The cost function contours of the noisy observations are overlaid as black lines and the new solution (and associated retrievals) is shown as a red triangle. This example shows that even small amounts of noise cause large shifts in the observed solution due to compensation between VOD and k along the diagonal curvature of the cost function. For only a single polarization the cost function moves up and down by a far smaller amount than the distance between the true and noisy solutions (not shown), but retrieving two variables simultaneously allows compensation between the two. This leads to large errors in retrieved VOD and k. Konings, Entekhabi, Chan, and Njoku (2011) performed an observing system simulation experiment (OSSE) in which the errors associated with different retrieval algorithms were tested over an area representing the United States by using known truth conditions and
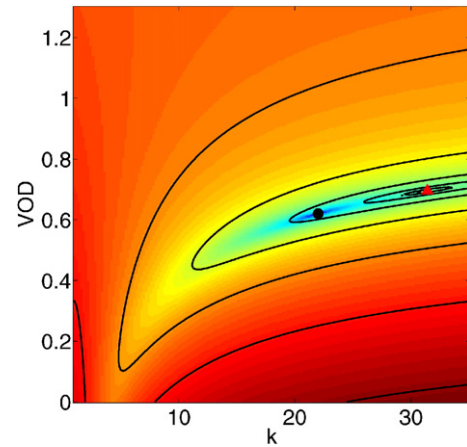

Fig. 1. Cost function J as a function of VOD and k for a sample set of observations (July 16th, 2012, for a pixel centered at 19.48°N, 103.53°W in Central Mexico). The 'true' solution of the cost function (without noise added) is shown by a black dot. A small amount of simulated noise is added to the observations, 0.005 for the H-pol and -0.002 for the V-pol. The contours of the resulting noisy cost function are shown as black lines. The noisy solution of the resulting cost function is shown by a red triangle and is far away from the true solution.

simulating observations with realistic parameterization, model, and observational errors. Both the bias and random errors of retrieved soil moisture increased several fold for a dual-channel algorithm relative to a single-channel algorithm due to compensating errors. This is consistent with the effect of observational errors tested in a smaller-scale OSSE (Crow et al., 2005), where dual-channel algorithm errors were also significantly higher than single-channel algorithm errors.

The problem of compensating errors can be reduced by using additional observations to increase the 'Degrees of Information' (the fractional degrees of freedom) (Konings et al., 2015) in the data used. The use of additional observations makes the retrieval problem less sensitive to noise. For sensors like SMAP where only a single incidence angle and frequency is available, this can be achieved by combining measurements from different overpasses. If the time between different overpasses is sufficiently short, vegetation properties can be assumed constant across the different overpasses. This assumption has also been used to improve multi-angular soil moisture retrievals from SMOS (Wigneron, Waldteufel, Chanzy, Calvet, & Kerr, 2000; Kerr et al., 2011). The soil dielectric constant varies much more rapidly than vegetation and must be retrieved separately for each overpass. Adding each additional overpass therefore increases the number of (correlated) observations by two, but the number of unknowns by only one (by assuming the same VOD, the only extra unknown is the new k).

3. Algorithm design

3.1. Moving window time series design

For each retrieval, the time series algorithm proposed in this work combines all observations within a moving window and retrieves a single value of VOD along with N different values of the dielectric constant k, where N is equal to the number of overpasses within the moving window. Thus, the retrieval is the solution to,

$$\min_{X=VOD,k_1,\dots,k_N} J(X) = \sum_{t=1}^{N} \sum_{p=H,V} \left(e_p^{obs} - e_p^{model}(X) \right)^2. \qquad (5)$$

The MT-DCA algorithm retrieves $N + 1$ independent parameters ($1 \times$ VOD and $N \times k$) with $2 \times N$ observations ($H \times N$ and $V \times N$). Increasing N increases the number of measurements available for the retrieval, but also increases the possible errors from changes in VOD over the time period spanning the observations (e.g. violations of the assumption

that VOD is constant across the N overpasses). The optimal choice of N is thus the minimum value such that the $2 \times N$ observations provide enough information to determine $N + 1$ parameters. Because the H- and V-polarized emissivities at any given pixel and time are correlated, however, they contain duplicate information and do not provide 2 full degrees of information for the retrieval. Instead, the measurements provide some fractional number of 'Degrees of Information' (DoI). The DoI is less than two by an amount depending on the non-linear correlation between the polarizations. It can be estimated using the normalized mutual information between the Aquarius-based polarized brightness temperatures. Here, the H- and V-polarized data together contain 1.86 Degrees of Information (Konings et al., 2015). Using measurements at independent days provides $1.86 \times N$ DoI. The DoI provide an upper bound on the number of parameters that can be estimated robustly from a given set of observations. Depending on the forward model and algorithm implementation, this bound may or may not be reached.

To find the minimum N that allows robust retrieval, the ratio of the total degrees of information divided by the total number of unknowns can be used. That is, the retrieval ratio $RR = 1.86 \cdot N/(N + 1)$. If RR is greater than 1, the retrieval algorithm is expected to be robust to noise. Fig. 2 plots RR for several values of N. The DoI and the resulting RR are also separately calculated for each land cover type by using only the Aquarius measurements over pixels of that land cover type. Because the non-linear relationship between the polarizations varies between land cover classes, the relationship between the two is weaker when data from multiple land cover types are combined. The DoI and RR therefore increase when calculated across all pixels rather than only those of a single land cover type. A choice of $N = 2$ is enough to get robust retrievals ($RR > 1$), so two overpasses are combined for this application.

At each pixel, two different values of VOD are retrieved for each overpass: once when the current overpass is the first of two in the moving window, and once when it is the second. Similarly, k is retrieved twice for each overpass and pixel depending on the location of the moving window. In each case, the two possible window positions are averaged to provide a single dataset of VOD and k. The two possible retrievals for each k (estimated from different multi-temporal windows associated with each overpass) will later be compared as a consistency check. Since Aquarius has a revisit time of 7 days (see Section 5.1), retrievals are only performed when there are at least two coincident observations in 14 days. This filters out times when missing data might otherwise affect the validity of the assumption that VOD is constant between data takes.
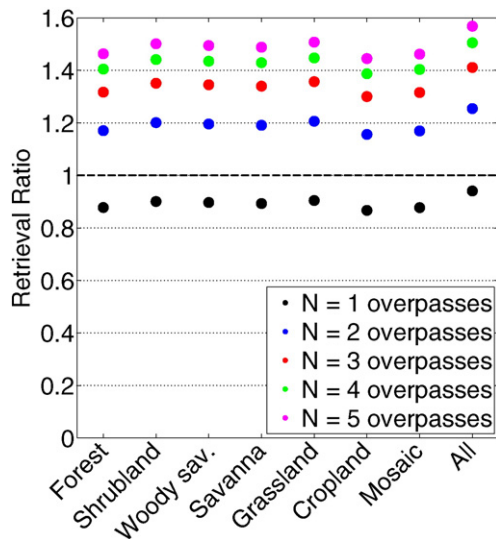
3.2. Albedo retrieval

Since the albedo is sensitive to canopy architecture and influences the retrieved values of VOD and k (Davenport et al., 2005), it is beneficial to retrieve its value directly instead of using an assumed dependence on land cover type. Such an assumption is sensitive both to errors in land cover classification (mostly based on optical data) and to vegetation variability within land cover types. It is possible to set up a retrieval approach wherein three overpasses are combined to retrieve 3 values of k_t, a constant VOD, and a constant ω. Such an approach has an $RR > 1$. However, the results illustrate the fact that the DoI only provides an upper bound that is not always reached — VOD and albedo compensate for each other significantly, leading to temporal fluctuations in retrieved albedo that are unrealistically large relative to its dynamic range and to its spatial variations (results not shown). The reason for such compensation can be understood by examining Eq. (1). The total brightness temperature can be separated into two components $T_B^{soil} = T_s(1 - r_p(k))\gamma$ and $T_B^{canopy} = T_c(1 - \omega)(1 - \gamma)(1 + r_p(k)\gamma)$. If the contribution from T_B^{soil} is small relative to the total and T_B^{canopy} dominates, the functional form of the effect of both ω and γ (which is a monotonic function of VOD) on the observed T_B is the same. It becomes impossible to distinguish between ω and VOD, causing large fluctuations in each. Fig. 3 shows the relative contribution of the T_B^{canopy} to the total brightness temperature under different ω and VOD. The contribution of T_B^{soil} to the total T_B is often small, especially over wet and heavily vegetated soils. This explains why allowing albedo to vary leads to unrealistically large temporal variations in both ω and VOD.

Instead, albedo is assumed constant (Van de Griend & Owe, 1994; Wigneron et al., 2004) and retrieved separately across the full record of observations (and alongside time-varying VOD and k). The retrieval of albedo is robust for a given pixel if the total DoI across the M VOD–k retrieval pairs throughout the time series ($M \cdot DoI \cdot N$) is greater than the total number of unknowns ($1 + M(N + 1)$). If two consecutive overpasses per VOD–k retrieval pair are used ($N = 2$), this requirement is met if more than two VOD–k retrievals are available ($M > 2$). If the total number of available retrieval pairs $M \leq 2$, no retrievals are attempted. Otherwise, all available observations for a given pixel are combined to find ω. The constant value of albedo is chosen that minimizes the sum of the optimal cost function for each retrieval pair,

$$
\begin{aligned}
X &= \min_{\omega} \left[\sum_{p=1}^{M} \min J \right] \\
&= \min_{\omega} \left[\sum_{p=1}^{M} \min_{k_{1t}, k_{2t}, VOD_t} \sum_{t=1}^{N} \sum_{p=H,V} \left(T_{B_p}^{obs} - T_{B_p}^{model}(X) \right)^2 \right].
\end{aligned}
\tag{6}
$$

Fig. 2. Retrieval ratio of degrees of freedom for the different land uses and varying number of dual-polarized observations.
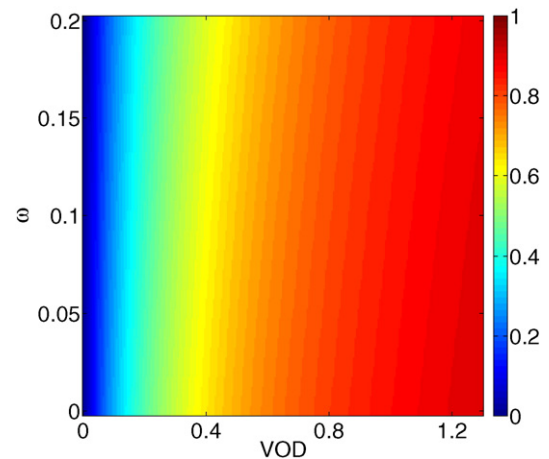

Fig. 3. Relative contribution of the vegetation canopy to the total brightness temperature emitted at H-polarization, $T_{B_H}^{canopy}/T_{B_H}$ as a function of albedo ω and VOD. A value of $k = 20$ is assumed. Results at V-polarization are qualitatively similar (not shown).

3.3. Additional parameters

The land surface temperature is determined from ancillary data as described in Section 5. In this paper, we further retrieve k from the rough-surface reflectivity for validation of the overall algorithm. The roughness parameter h is assumed to be equal to 0.13, the average of the different land-cover dependent values assumed by SMAP (O'Neill et al., 2012).

4. Methods

The MT-DCA algorithm is applied to three years of data from the NASA Aquarius sensor. While an alternative version of MT-DCA could be build that retrieves soil moisture directly instead of the soil dielectric constant k, here we retrieve soil dielectric constant in order to estimate parameters that are entirely independent of ancillary data (such as soil texture), which might contain errors. A similar approach was previously used by de Jeu, Holmes, Parinussa, and Owe (2014). The search space for k is limited between 2.5 and 35, values that were chosen based on the Mironov dielectric mixing model (Mironov, Dobson, Kaupp, Komarov, & Kleshchenko, 2004) for a range of soil types. For VOD, the search space is limited to values between 0 and 1.3 Np. Validation of the resulting VOD retrievals using direct ground-based measurements of vegetation water content is difficult, as no regional monitoring networks exists at the spatial scale of the Aquarius satellite. Vegetation water content is highly spatially variable, so that any in situ measurements that cover only a small fraction of the total Aquarius instrument field-of-view scale cannot be considered representative. It is therefore difficult to directly validate VOD data. Instead, the spatial patterns of the retrieved datasets are examined for physical realism. Additionally, several focus pixels are chosen that represent relatively homogeneous land cover conditions (measured using the Gini–Simpson index; Simpson, 1949) on the discrete land cover classes, as proposed in Piles, McColl, Entekhabi, Das, and Pablos (2015) and a wide variety of climatic and land cover conditions. One of the SMAP Core Cal/Val sites (SMAPEx) is also chosen as a focus pixel. The specific location and dominant land cover type of each focus pixel are included in Table 1. The temporal dynamics of each of these focus pixels are compared to the temporal dynamics of precipitation over the same area, which is expected to have a strong influence on vegetation water content in many regions.

The MT-DCA VOD retrievals are also compared to those from the commonly used LPRM algorithm (Owe et al., 2001, 2008; Meesters et al., 2005). In order to be able to distinguish algorithm differences from differences in frequency or sensor characteristics, the LPRM algorithm is implemented and applied to the same Aquarius observations used for the MT-DCA. The implementation of LPRM used here retains the core features of the LPRM algorithm: an analytical relationship is used to predict VOD based on the Microwave Polarization Difference Index (MPDI), emissivity, and albedo (which is assumed to have a constant global value known a priori). The cost function retains only the H-polarized brightness temperature. Note, however, that there are small differences remaining between this study's LPRM algorithm

implementation and recent L-band retrievals with LPRM applied to SMOS (Van der Schalie, Parinussa, et al., 2015; Van der Schalie, Kerr, et al., in press). In particular, our implementation of the LPRM algorithm for Aquarius data does not use a soil moisture-dependent roughness formulation, retrieves a dielectric constant instead of soil moisture, and does not combine modeled land surface temperatures from multiple depths. The soil treatment is kept the same between the MT-DCA and the LPRM algorithm in order to isolate and clarify the effects of the new multi-temporal optical depth and albedo treatment in MT-DCA. We also keep values of VOD > 0.35 for the analysis instead of removing them as in Van der Schalie, Kerr, et al. (in press), as this would remove retrievals over much of the globe. None of these factors have an impact on the qualitative results of the comparison here, e.g. the relative noise levels of MT-DCA and LPRM (see Section 6). For the LPRM algorithm, $\omega = 0.12$ is assumed, based on the value in Van der Schalie, Kerr, et al. (in press).

Aquarius data are used because it provides both collocated radar and radiometer observations. This study also explores the relationship between Aquarius MT-DCA VOD and two alternative active vegetation indices. Because soil scattering generally leads to negligible depolarization (Van Zyl & Kim, 2011), the cross-polarized backscattering coefficient can be used as an index of vegetation scattering intensity and water content. Alternatively, Arii, Zyl, Kim, Member, and Current (2010) defined the Radar Vegetation Index (RVI), which is a measure of the randomness of canopy elements and vegetation scattering.

Although the retrieved VOD dataset is the primary focus of this study, the MT-DCA retrievals are further evaluated by analyzing the retrieved values of ω and k. The spatial and temporal patterns of the retrievals of k are also compared to those of LPRM. To avoid contamination from differences in assumed soil texture and dielectric mixing, the retrievals of the dielectric constant k are compared rather than the soil moisture estimates. The two are monotonically related. Lastly, a consistency check is performed on the k retrievals. For each date and location, two retrievals of k are obtained — one when the current date is the first in the two-overpass window, and one when it is the second. The two sets of retrievals are compared to test the robustness of the retrievals.

Soil roughness is often assumed to depend on land cover type, as in the SMAP retrieval algorithm (O'Neill et al., 2012) or retrieved from additional information, as done by SMOS (Kerr et al., 2011). In this study, we use a globally constant soil roughness value of $h = 0.13$ and $n = 2$, the average of the land-cover dependent values used in the SMAP retrieval algorithm (O'Neill et al., 2012). Using a globally constant value allows the algorithm retrieval test to be independent of any possible errors in ancillary land cover data. As a result, any spatial patterns in the retrievals (see Section 6) are a direct result of the data retrievals and not of ancillary data. Sensitivity tests showed that the exact value of soil roughness used had only a minor effect on the retrieved VOD and albedo values. To isolate the effects of the unique albedo and VOD retrieval assumptions of the MT-DCA, the same roughness assumptions are used for both the MT-DCA and LPRM algorithm implementations.

The different datasets used for these analyses are described in Section 5. All datasets are converted to the same gridding scheme and spatial resolution, which is chosen to match the Aquarius observations. Since Aquarius measurements do not exactly overlap over time, the first 7 days of observations are used to set up the grid. Subsequent overlapping footprints with centers less than 0.15° from a grid center are included in that grid cell, otherwise they are excluded. More detailed information on the gridding strategy can be found in McColl, Entekhabi, and Piles (2014) and Piles et al. (2015). To enable spatial and temporal consistency, all data sets used in this work have been resampled to the Aquarius footprint grid: land-cover classification data (used in interpreting the results only) is resampled using the most common land cover class, while ancillary precipitation and temperature data are resampled using linear averaging. When converting datasets with a higher spatial resolution to the Aquarius gridding scheme, a circular orbital footprint is assumed, with a radius dependent on latitude. Note

Table 1
Target areas: name, location, and dominant IGBP land cover type.

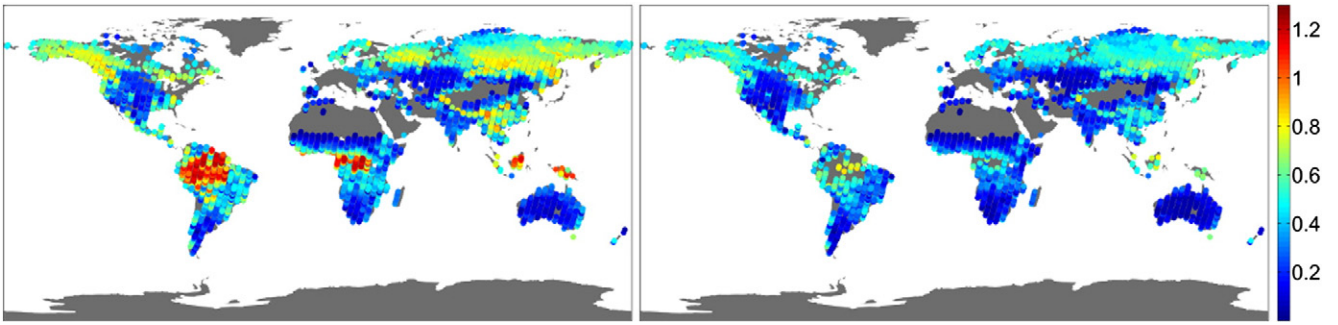| Site name	Latitude	Longitude	Land cover
SMAPEx	34.70°S	145.73°E	Open shrubland
Amazon	2.23°S	66.00°W	Evergreen broadleaf forest
Nordeste	7.30°S	42.63°W	Savanna
Pampas	33.82°S	60.17°W	Cropland
East Africa	5.49°S	34.50°E	Woody savanna
Central Asia	45.27°N	66.30°E	Grassland
West Africa	9.68°N	6.37°E	Natural vegetation mosaic

Fig. 4. Global maps of mean MT-DCA (left) and LPRM (right) VOD retrievals for the three year period of this study.

that the land cover data are only used in the analysis of the results, not in the retrieval algorithm itself.

5. Datasets used

5.1. Aquarius Level 2 data

The Aquarius/SAC-D mission, launched in June 2011, is a joint U.S.–Argentinian mission to map the surface salinity field of the oceans from space. It has equatorial crossing times of 6 A.M. (descending) and 6 P.M. (ascending) and a 7-day repeat cycle. Its payload includes the NASA Aquarius sensor, the first combined active/passive polarimetric L-band microwave instrument in space. It consists of three L-band radiometers and a scatterometer, which image the Earth in a pushbroom

fashion at 29.36° (inner beam), 38.49° (middle beam), and 46.29° (outer beam) incidence angles, with 3 dB footprints of 76 × 94 km, 84 × 120 km and 96 × 156 km (Le Vine et al., 2007).

The present study uses three years of global Aquarius Level 2 data (version 2.0), covering the period from September 1st, 2011 to August 31st, 2014. Dual-polarized brightness temperatures (T_{BH} and T_{BV}) from the middle beam acquired during morning (descending) overpasses are used for joint VOD, k, and ω retrievals. Coincident cross-polarized backscattering coefficients (σ_{HV}) are also selected to explore their relationship with retrieved VOD. Only data from morning overpasses are used to ensure the vegetation and near-surface soil are in thermal equilibrium. Data from the central beam is chosen since, out of the three available beams, the greatest amount of independent information can be obtained from the center-most angle at 38.49°, which is also the
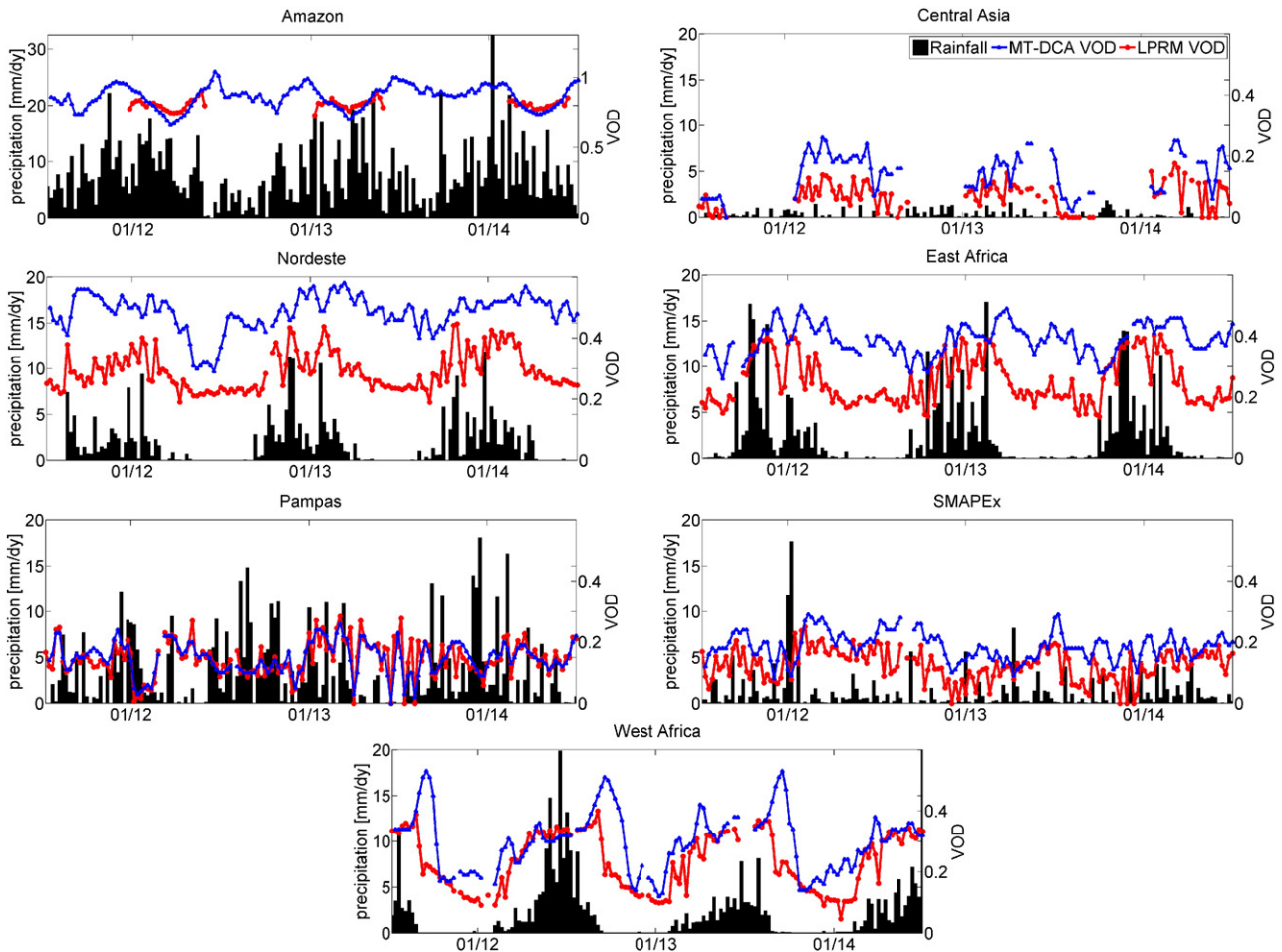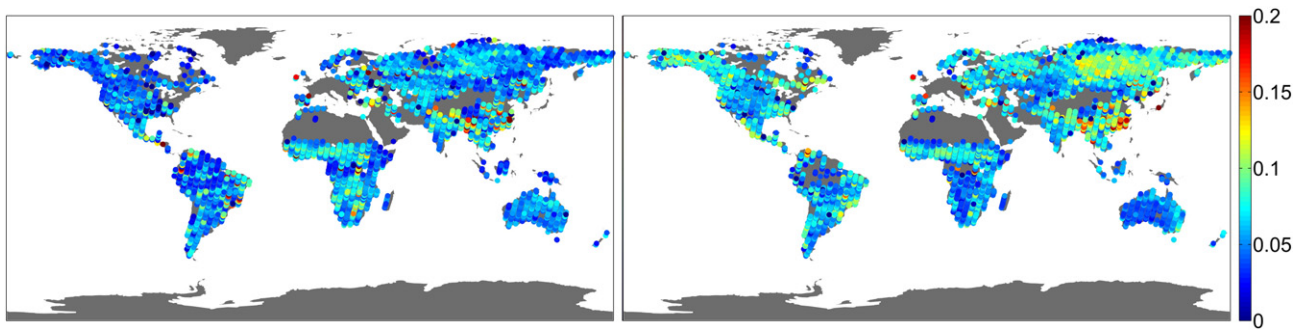

Fig. 5. Time series of weekly mean MT-DCA VOD, LPRM VOD, and precipitation over focus pixels. Note the different axes scale for the Amazon series.

Fig. 6. Global maps of standard deviation of MT-DCA (left) and LPRM (right) VOD retrievals for the three year period of this study. In both cases, a 5-week moving average is first removed from the time series for each pixel, so that the standard deviation primarily reflects high-frequency variability.

closest to SMAP's incidence angle. Radar and radiometer data have been screened for orbital maneuver times and Radio Frequency Interference (RFI) (Le Vine, De Matthaeis, Ruf, & Chen, 2014). In addition, data over ocean, land–sea transitions, Antarctica, Greenland and non-vegetated surfaces (water, urban and barren land covers) have been masked out.

5.2. NCEP land surface temperatures and flags

The land surface temperature T provided as auxiliary information with Aquarius data is used as an input retrieval parameter in the present study. They are obtained from the National Centers for Environmental Prediction (NCEP) Global Data Assimilation System (GDAS) and interpolated from the daily 0.25° product to the exact time and location of the Aquarius observations. Pixels with land surface temperatures less than 0 °C were assumed to have frozen soils and masked out of the analysis. Similarly, pixels where the observed emissivity was greater than one were assumed to have an erroneous land surface temperature and masked. Lastly, locations and times where NCEP data suggest the presence of snow or ice cover were also removed from the analysis.

5.3. MODIS IGBP land cover

The 2005 MODIS MCD12Q1 International Geosphere-Biosphere Programme (IGBP) collection 5 land cover product has been used in this study to characterize the dominant land cover within each Aquarius footprint. The MODIS IGBP land cover is a world-wide product at 500-m spatial resolution that encloses 17 distinctive land cover classes. MODIS products are freely distributed by the U.S. Land Processed Distributed Active Archive Center (www.lpdaac.usgs.gov). Note that land cover

data are only used to interpret the results and not within the retrieval algorithm.

5.4. MERRA-Land observation-corrected global precipitation

Global daily precipitation data from the Modern Era Retrospective Analysis (MERRA)-Land run (Reichle et al., 2011) have been used in this study, with additional corrections applied to match the data from the Global Precipitation Climatology (GPCP) project and the NOAA Climate Prediction Center (CPC) (Reichle & Liu, 2014).

5.5. Water fraction

The observed brightness temperatures from Aquarius are corrected for the effect of emission from surface water bodies. The NCEP Land Surface Temperature is assumed to be equal to the temperature of any water bodies in the pixel, whose brightness temperature $T_{B_p}^{water}$ is calculated using the model of Klein and Swift (1977) with an assumed salinity of 0.5 ppt. The fractional coverage of water bodies in the pixel f_w is then used to separate the land emission and water emission contributions to the Aquarius observations. It is assumed that $T_{B_p}^{obs} = f_w T_{B_p}^{water} + (1 - f_w) T_{B_p}^{land}$, which can be re-arranged to solve for $T_{B_p}^{land}$. The static water fraction f_w is determined by calculating what fraction of the high-resolution 250 m land cover data from the MODIS MOD44W dataset are classified as water or land. The data are first aggregated to the 3 km EASE grid used in the SMAP Testbed and then converted to the Aquarius footprint grid. Pixels with more than 10% static water cover were removed from the analysis entirely.
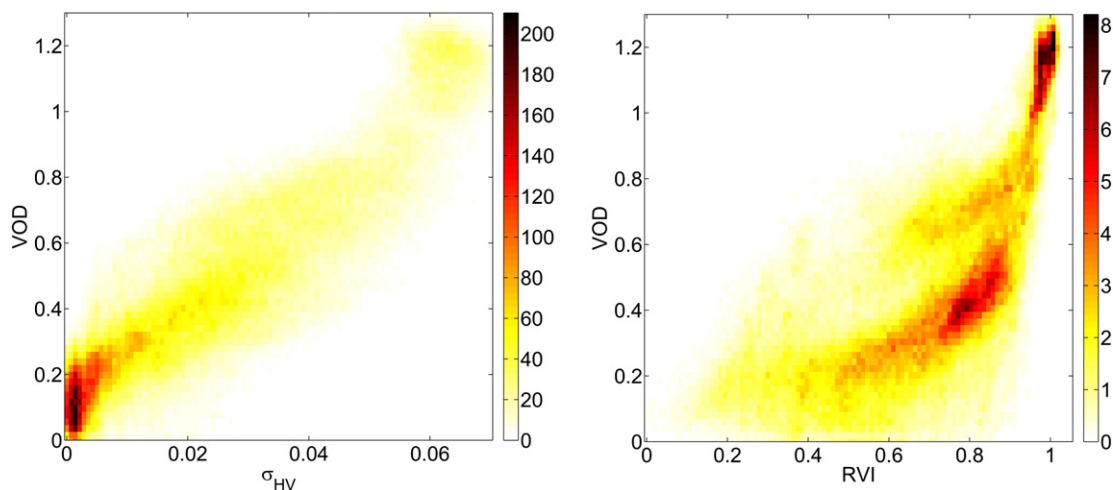
Fig. 7. Joint density of Aquarius radiometer-derived vegetation optical depth vs. scatterometer σ_{HV} in linear units (left) and radar vegetation index (right). All available combinations of active and passive measurements (e.g. one at each location and time) were used.

Table 2
Land cover variability of retrieved albedo *w*. Parameters for SMAP ω are obtained from O'Neill et al. (2012).

Land cover type	SMAP ω	Retrieved: mean (std. dev.)
Evergreen needleleaf forest	0.12	0.05 (0.02)
Evergreen broadleaf forest	0.12	0.05 (0.03)
Deciduous needleleaf forest	0.12	0.06 (0.02)
Deciduous broadleaf forest	0.12	0.03 (0.03)
Mixed forest	0.10	0.05 (0.03)
Closed shrublands	0.05	0.03 (0.04)
Open shrublands	0.05	0.05 (0.05)
Woody savannas	0.12	0.04 (0.03)
Savannas	0.08	0.02 (0.03)
Grasslands	0.05	0.03 (0.05)
Croplands	0.05	0.04 (0.04)
Cropland/natural veg. mosaic	0.065	0.02 (0.03)

6. Results

6.1. VOD retrievals

A global map of three-year time-average Aquarius VOD retrievals using the MT-DCA is shown in Fig. 4. The spatial patterns of VOD retrievals follow global vegetation distributions, with the highest vegetation optical depth in tropical and boreal forests and low VOD in arid climates. Across the Sahel, there is a gradient of increasing average VOD from North to South. Fig. 4 also shows the mean VOD obtained by applying the LPRM algorithm. The spatial patterns of the two VOD temporal means are generally consistent except over densely forested areas, where MT-DCA values of VOD are higher than those of the LPRM algorithm. This is consistent with the fact that the MT-DCA retrieved values of the effective single-scattering albedo are generally lower than the value of $\omega = 0.12$ used by the LPRM algorithm (see Section 6.2). Over tropical densely forested areas, the MPDI is often too small for valid LPRM retrievals (only 32% of MT-DCA retrievals in this region also allow a valid retrieval with the LPRM algorithm), so that the mean LPRM plot in Fig. 4 may also be sampling a different subset of the seasonal cycle than the annual average of MT-DCA, increasing the difference between the two. Across the globe, the LPRM algorithm predicts a negative VOD for 5% of retrievals, which is physically impossible. These occur predominantly over dry, lowly vegetated ecosystems. Indeed, for regions where MT-DCA predicts a VOD less than 0.1, more than 50% of all LPRM VOD retrievals are negative. These unphysical values occur because the LPRM algorithm assumes a fixed relationship between *k* and VOD based on an exact equality of the $\tau - \omega$ model in both polarizations. In reality, noise and model error (including, for example, an imperfect ω specification) may mean that there is no perfect solution to both equations, so after a least-error value of *k* is found the accompanying VOD may not be physically realistic. For a

relatively coarse resolution (90 km footprint) satellite like Aquarius, this may be especially common. The occurrence of negative VOD retrievals at L-band is consistent with a previous C-band application of LPRM in which switching from soil moisture retrievals with possibly noisy soil texture values to soil dielectric constant retrievals increased the number of valid VOD retrievals by as much as 200 days a year, again predominantly over dry areas (de Jeu et al., 2014). In this paper, LPRM algorithm retrievals that predict a negative VOD are removed from the comparison. For an additional 10% of global observations with valid MT-DCA retrievals, including many over the Amazon and Congo river basins, LPRM retrievals are not made because they have a MPDI of less than 0.01 (Meesters et al., 2005).

To gain further insight into the behavior of the MT-DCA retrievals, their temporal dynamics are compared to those of LPRM VOD retrievals and of precipitation (an expected strong predictor of VOD in several areas) for several focus pixels in Fig. 5. The pixels are described in Table 1. All datasets are shown at a weekly temporal resolution, equal to the average revisit time of the Aquarius satellite. In cases where there is significant seasonal variability in precipitation, the retrieved VOD is responsive to accumulated precipitation and consistent with expected seasonal changes in vegetation water content. For example, a clear seasonal cycle is evident in the VOD retrievals over West Africa, Nordeste, and East Africa, where VOD shows a steady decline after the end of the rainy season. In each of these sites, there is a lag between the end of the rainy season and the minimum value of VOD. This suggests that VOD is sensitive to changes in vegetation water content accompanying the plant response to water stress and/or to changes in leaf biomass — the response of vegetation to a reduction in (stochastic) rainfall is not instantaneous. For most target regions, the LPRM algorithm VOD shows more high-frequency variability than the MT-DCA VOD. Although it is possible that the constant VOD assumption in the MT-DCA slightly dampens natural variability, the near-oscillatory behavior of many of the high-frequency LPRM algorithm retrievals suggest that they are due to retrieval noise rather than due to true variability in the signal. Such differences in temporal behavior occur over much of the globe, as shown in Fig. 6. For both MT-DCA and LPRM, the standard deviation is shown after the 5-week moving window mean is removed. This moving window subtraction acts as a high-pass filter, and the remaining variability is more likely to be retrieval noise than true temporal variability in the signal. The MT-DCA high-frequency variability is significantly lower than that of LPRM algorithm for much of the globe. The high-frequency variability of the L2 VOD from SMOS (which uses multi-angular measurements to determine VOD and whose cost function also includes a prior based on leaf area index) (Kerr et al., 2011) is about halfway between that of MT-DCA and that of LPRM (not shown).

The availability of both active and passive data from Aquarius allows a preliminary investigation of active and passive vegetation indices.
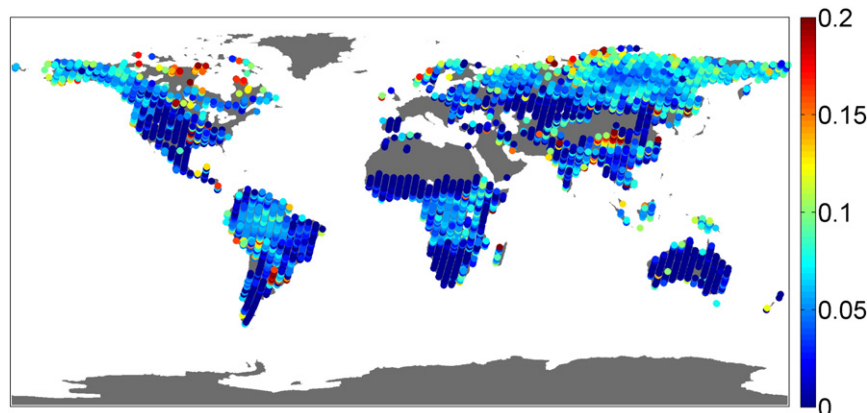

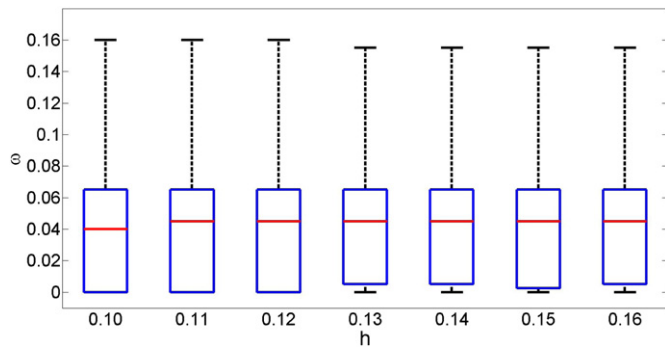**Fig. 8.** Global map of retrieved albedo.

Fig. 9. Boxplot of global albedo distribution as a function of the constant value assumed for the roughness parameter h.

Fig. 7 compares Aquarius MT-DCA VOD data to coincident σ_{HV} and RVI observations by showing the joint density of the two for all locations and times. The VOD–RVI joint density ($R^2 = 0.46$) is more flat and has longer tails than that of VOD and σ_{HV} ($R^2 = 0.76$). That is, there is more scatter in the relationship between VOD and RVI than in that between VOD and σ_{HV}. This suggests the latter may hold more promise as an active-microwave-based predictor of VOD for single-channel soil moisture retrieval approaches. However, some saturation in the σ_{HV} may be occurring for densely vegetated sites.

6.2. Albedo retrievals

Table 2 shows the average retrieved albedo values for each land cover type, as well as the average parameters assumed in the SMAP passive-only retrieval algorithm. The retrieved values are generally lower than the land-cover dependent values published as preliminary values by SMAP (O'Neill et al., 2012), consistent with theoretical findings that higher-order scattering reduces the effective albedo values used in the tau–omega model (Kurum, 2013). Albedo values are generally higher for vegetation covers with significant woody components, such as forests and woody savannas. However, there is significant variability in retrieved albedo values across and within land cover classes. Grasslands, croplands, open shrublands, and savannas show particularly large amounts of variability within each class relative to the class average. For open shrublands, this variability appears to be due to differences between the tundra regions and shrublands in less densely vegetated areas.

A global map of the retrieved constant albedo values is shown in Fig. 8. Not surprisingly, the spatial patterns of albedo roughly follow those of average VOD and of expected vegetation cover, although there are a few more noisy high-albedo outliers. In general, the

transition between low and high vegetation regions is more rapid for albedo than for VOD, as can be seen for example in Northern Africa. This is consistent with the apparent sensitivity of albedo to woody biomass; average VOD trends may be capturing smaller-scale spatial variations in leaf cover that albedo is insensitive to.

When the transmissivity γ is high, the $\tau - \omega$ model predicts that observed brightness temperatures are sensitive to both the quantities $1 - r_p^*$ and $1 - \omega$. There may thus be some concern that the retrieved values of ω will be sensitive to the assumed soil roughness value h (here taken to be globally constant). Fig. 9 shows that there is very little sensitivity of the retrieved ω to the assumed value of soil roughness, likely because errors in h can partially trade off with errors in k.

6.3. k retrievals

For each date and location, k can be retrieved at either the start or the end of the moving window. A global map of the time-average of the instantaneous difference between the two sets of k retrievals is shown in Fig. 10. The difference is generally small, as confirmed by the figure inset, which shows the overall distribution of differences. The standard deviation between the differences is only 1.54 and there is no significant bias (mean $\Delta k = 0.10$). The similarity between the two sets of k confirms the robustness of the algorithm for soil moisture, VOD, and albedo retrievals.

Fig. 11 shows the mean retrieved k for both the MT-DCA and LPRM algorithms. The MT-DCA dielectric constants are slightly higher (wetter soils) than those of the LPRM algorithm for much of the globe. In regions such as southeastern China, Russia, Scandinavia and Bolivia/Matto Grosso, there is significantly more spatial variability in the mean LPRM retrievals than in the MT-DCA ones. Over much of the Amazon and Congo basins, LPRM retrievals are not valid because the MPDI is not sufficiently large (Meesters et al., 2005). There are a few pixels in the Amazon where the average LPRM k is much higher than for MT-DCA, but this is probably a mixture of higher LPRM retrievals and the fact that LPRM retrievals are not valid during many times of the year, so that the two averages may represent different seasonal cycles. When the LPRM algorithm is applied to Aquarius with albedo values from MT-DCA instead of the LPRM assumed value of 0.06 (Owe et al., 2008), the difference in average k reduces to near-zero values for the vast majority of pixels (not shown), suggesting that the ability to retrieve albedo is an important component of the MT-DCA algorithm for soil moisture retrievals. The effect of the albedo assumption is smaller for VOD retrievals than for k retrievals, but also significant.

Time series of MT-DCA and LPRM k retrievals over the focus pixels for the study period are shown in Fig. 12. The temporal dynamics of retrievals from both algorithms are very similar, though there is a slight bias between the two in many cases. In the Amazon pixel, the seasonal
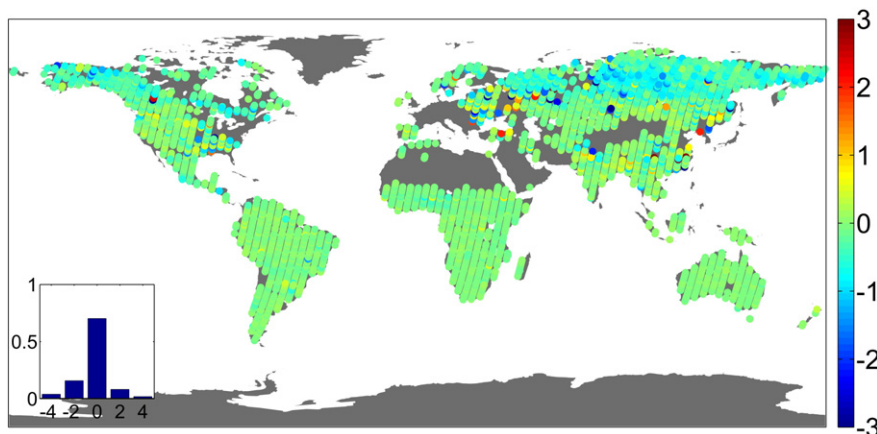

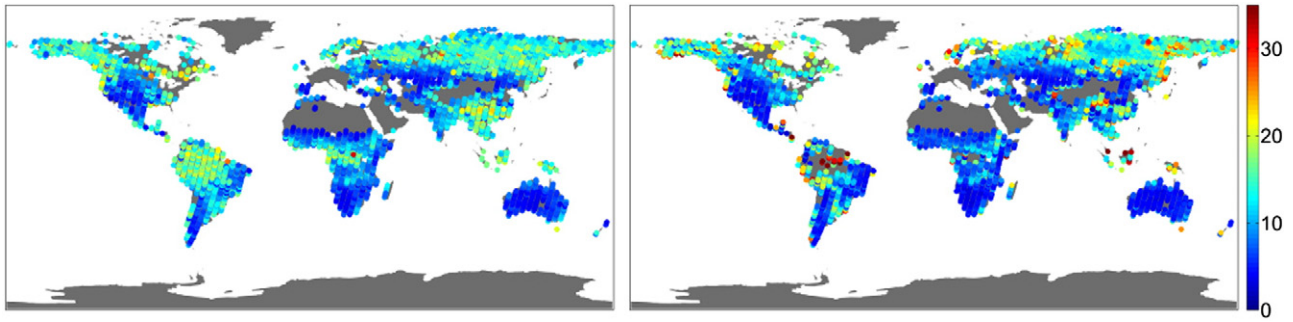**Fig. 10.** Mean difference between the two sets of k retrieval.

Fig. 11. Global maps of temporal mean *k* retrieval for Aquarius (left) and LPRM (right).

cycle in soil dielectric constant is considerably larger than that of VOD (Fig. 5), consistent with the fact that forests in this region access deep stores of groundwater (Baker et al., 2009). Long drydowns in West Africa and Nordeste occur more slowly for MT-DCA than for LPRM, though it is difficult to say which is more accurate at these large scales.

7. Discussion and conclusions

A new method, the multi-temporal dual channel algorithm (MT-DCA), is proposed to retrieve microwave vegetation optical depth (VOD), the effective single-scattering albedo ω, and soil dielectric constant (monotonically related to soil moisture) from time-series of dual-polarized L-band radiometer observations. It is applied to three years of Aquarius data at L-band. The algorithm relies on the premise

that vegetation changes more slowly than soil moisture. A moving average window is used to combine observations from two overpasses while retrieving only a single constant value of VOD alongside the dielectric constant for each of the two overpasses. Single-scattering albedo is assumed to be constant in time and optimized separately across the full record of observations. Note that when soil moisture conditions are similar during the two overpasses, observations from the second overpass do not provide additional information and can lead to noisy retrievals. For Aquarius applications, using 3 overpasses or more leads to a moving window size of 21 days or more, over which the assumption of constant vegetation may not hold. For other satellites with a more frequent revisit time, using a slightly longer window can increase the chance that soil moisture conditions change significantly during the moving window time period, adding additional
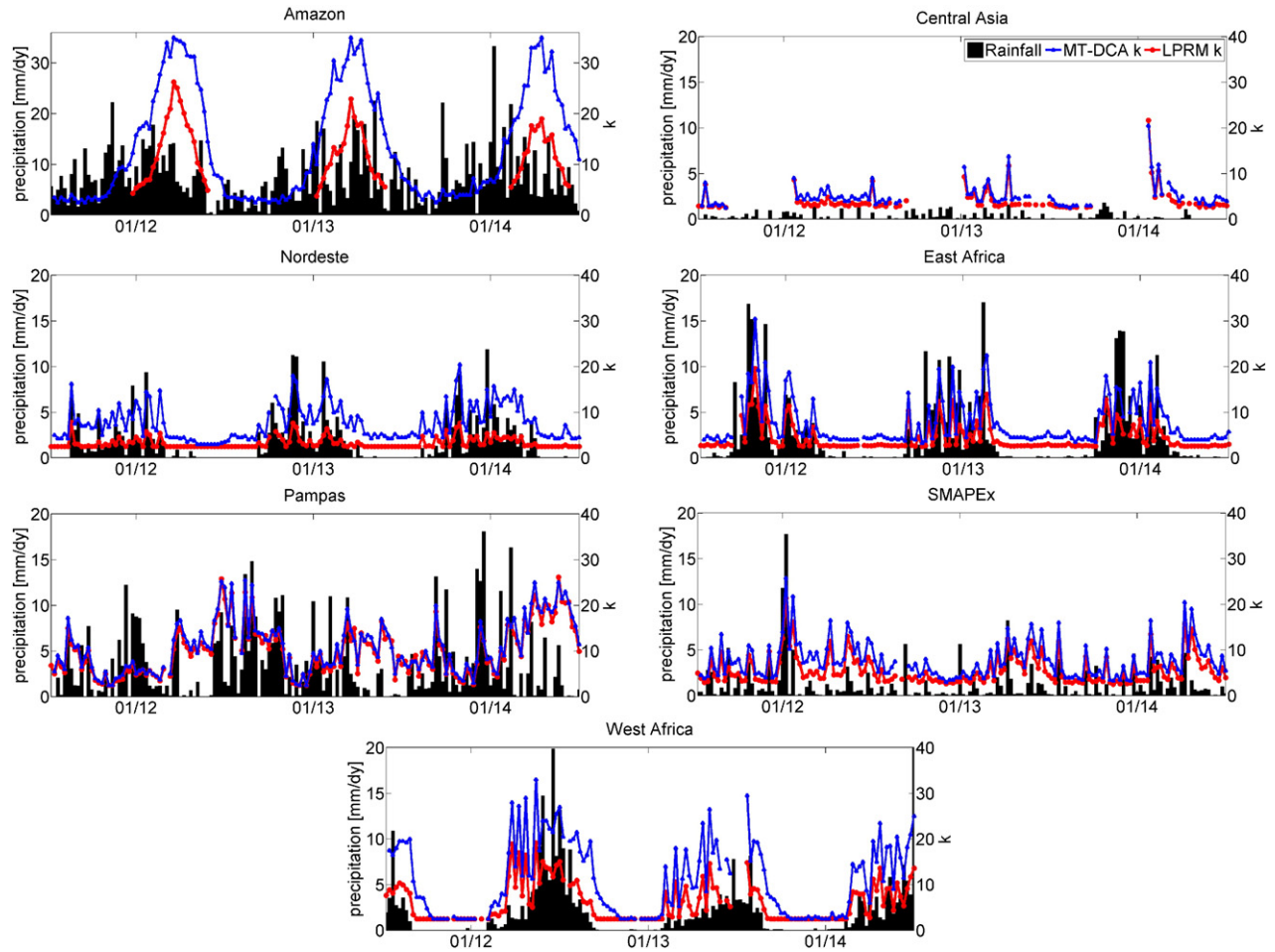

Fig. 12. Time series of weekly mean MT-DCA *k*, LPRM *k*, and precipitation over focus pixels. Note the different axes scale for the Amazon series.

information to the measurements. Future work is needed to investigate whether such variations can improve the quality of MT-DCA retrievals for other satellites such as SMOS and SMAP, whose more frequent revisit time is likely to lead to improved performance of MT-DCA. Another limitation of the MT-DCA algorithm is that it cannot capture sudden changes in VOD such as those that might be induced by fire or deforestation during the time when the moving window passes over the destruction event. However, such an event may still be detectable with some delay when there is a large change in VOD over a small number of moving windows.

The proposed multi-temporal algorithm retrieves microwave scattering albedo alongside VOD and soil dielectric constant rather than requiring an a priori assumption on its value based on land cover as is commonly done. This not only improves the quality of the VOD and k retrievals, but also allows simultaneous retrieval of the effective single-scattering albedo. Albedo is assumed to be constant in time, consistent with prior literature and the fact that it is strongly dependent on canopy architecture.

Almost all existing studies of measured single scattering albedo or effective scattering albedo have been based around results from airborne or tower-based studies with limited spatial coverage. Du, Kimball, Jones, and Member (2015) calculate empirical relationships for albedo by using spaceborne AMSR-E observations, but it does so by comparing to in situ data that will likely contain significant representativeness errors. Rahmoune, Ferrazzoli, Kerr, and Richaume (2013) use multi-angular data from SMOS but is limited to forests. In this study, we present the first global map of L-band albedo determined from spaceborne observations. The retrieved values of single-scattering albedo are low, but non-zero. The albedo is largest across land cover conditions with significant woody components. The forested regions in South America are found to have a lower albedo than those of the Northern Hemisphere, consistent with Rahmoune et al. (2013). In almost 95% of cases, the retrieved albedo value is lower than the value that would have been assigned by the land cover-based parameterization in the SMAP ATBD (O'Neill et al., 2012). There are large variations in albedo even within a given land cover class, suggesting the common assumption of a land-cover based albedo value is rather poor. Indeed, for the closed shrublands, savannas, grasslands, croplands, and cropland/natural vegetation mosaic classes, the variability of albedo across land cover is larger than its average value. When LPRM is run with albedo values retrieved from the MT-DCA, much of the difference in dielectric constant retrievals disappears. Although it is difficult to validate the retrievals in this paper, given the likely errors in prior assumptions of albedo, the significant effect of albedo on k retrievals suggests that the ability of MT-DCA applications to retrieve it alongside other variables is a major advantage.

The new VOD estimates have temporal dynamics that are consistent with precipitation and prolonged dry-downs, and both canopy water retention and biomass drying and wilting processes are reflected in the VOD retrievals. This confirms that VOD is a vegetation indicator that can be complementary to well known visible infrared indices such as NDVI and LAI. The MT-DCA Aquarius retrievals of VOD show significantly less high-frequency temporal variability due to noise than those from LPRM applied to Aquarius brightness temperature data. Additionally, because of the fixed relationship between VOD and k assumed by LPRM in the presence of noisy observations, LPRM retrievals lead to unphysical predictions of negative VOD or invalid retrievals in 16% of cases. The MT-DCA does not suffer from this problem.

At higher frequencies, brightness temperatures are less sensitive to soil moisture and have less penetration through the canopy than at L-band. Nevertheless, retrieval algorithms using temporal snapshots are still prone to measurement noise. Using a method with time series such as the one proposed in this paper may also lead to some improvements in VOD retrieval accuracy at C, X and Ku-bands. The VOD represents an integrated value over the canopy, weighted depending on the rate of attenuation of the signal through the canopy. This attenuation rate is dependent on both the frequency band of the measurement and the canopy properties themselves. As a result, the canopy properties and height ranges that dominate the signal at a given frequency band vary by location. This complicates interpretation of VOD data, as water stress in both branches and leaves as well as canopy structure (which affects the b-parameter) both vary with canopy height. Additional work is needed to better understand the effect of measurement frequency on VOD retrievals and interpretation.

Overall, VOD estimates obtained using the proposed algorithm have temporal dynamics that are generally consistent with precipitation and prolonged dry-downs. Both canopy water retention and biomass drying and wilting processes are reflected in the VOD retrievals. This suggests optical-infrared indices such as NDVI and LAI, which are not directly sensitive to vegetation water content, are a poor basis for VOD in soil moisture retrieval algorithms. Indeed, other studies of VOD (Jones, Jones, Kimball, & McDonald, 2011; Lawrence et al., 2014) have found that the end-of-season VOD variability is distinct from the signal found in optical-infrared vegetation indices. By contrast, a comparison of MT-DCA VOD with collocated radar observations (σ_{HV}) shows there is a strong relationship between the two microwave measures of vegetation. The σ_{HV} is a better predictor of VOD than RVI (Fig. 7). This may be relevant to the design of multi-resolution active–passive vegetation retrievals from upcoming SMAP data. SMAP plans to use Normalized Difference Vegetation Index (NDVI) climatology from MODIS as ancillary dataset for VOD in its baseline soil moisture retrieval algorithm. With the proposed algorithm, SMAP independent VOD retrievals could be used to improve SMAP soil moisture retrievals. This study further suggests that cross-polarized backscatter signals, which will be gathered at higher spatial resolution than radiometric measurements by SMAP. The proposed method could be applied to SMOS and SMAP L-band data to better quantify the contribution of the vegetation to total emissivity and therefore improve soil moisture retrievals.

Acknowledgments

References

Andela, N., Liu, Y. Y., van Dijk, A. I. J. M., de Jeu, R. A. M., & McVicar, T. R. (2013). Global changes in dryland vegetation dynamics (1988–2008) assessed by satellite remote sensing: Comparing a new passive microwave vegetation density record with reflective greenness data. Biogeosciences, 10(10), 6657–6676.

Arii, M., Zyl, J. J. V., Kim, Y., Member, S., & Current, A. (2010). A general characterization for polarimetric scattering from vegetation canopies. IEEE Transactions on Geoscience and Remote Sensing, 48(9), 3349–3357.

Baker, I. T., Prihodko, L., Denning, A. S., Goulden, M., Miller, S., & Da Rocha, H. R. (2009). Seasonal drought stress in the Amazon: Reconciling models and observations. Journal of Geophysical Research – Biogeosciences, 114(1), 1–10.

Bindlish, R., Jackson, T., Cosh, M., Zhao, T., & O'Neill, P. (2015). Global soil moisture from the Aquarius/SAC-D satellite: Description and initial assessment. IEEE Geoscience and Remote Sensing Letters, 12(5), 923–927.

Bohrer, G., Mourad, H., Laursen, T. A., Drewry, D., Avissar, R., Poggi, D., ... Katul, G. G. (2005). Finite element tree crown hydrodynamics model (FETCH) using porous media flow within branching elements: A new representation of tree hydrodynamics. Water Resources Research, 41(11) (n/a–n/a).

Ciais, P., Sabine, C., Bala, G., Bopp, L., Brovkin, V., Canadell, J., ... Vesala, T. (2013). Climate change 2013. The physical science basis. Contribution of Working Group 1 to the fifth assessment report of the Intergovernmental Panel on Climate Change (pp. 465–570). New York: Cambridge University Press (Ch. Carbon and).

Crow, W. T., Chan, S. T. K., Entekhabi, D., Houser, P. R., Hsu, A. Y., Jackson, T. J., ... Zhan, X. (2005). An observing system simulation experiment for Hydros radiometer-only soil moisture products. IEEE Transactions on Geoscience and Remote Sensing, 43(6), 1289–1303.

Cui, Q., Shi, J., Du, J., Zhao, T., & Xiong, C. (2015). An approach for monitoring global vegetation based on multiangular observations from SMOS. *IEEE Journal of Selected Topics in Applied Earth Observations and Remote Sensing, 8*(2), 604–616.

Davenport, I., Fernandez-Galvez, J., & Gurney, R. (2005). A sensitivity analysis of soil moisture retrieval from the tau–omega microwave emission model. *IEEE Transactions on Geoscience and Remote Sensing, 43*(6), 1304–1316.

de Jeu, R. a. M., Holmes, T. R. H., Parinussa, R. M., & Owe, M. (2014). A spatially coherent global soil moisture product with improved temporal resolution. *Journal of Hydrology, 516*, 284–296.

Du, J., Kimball, J. S., Jones, L. A., & Member, S. (2015). Passive microwave remote sensing of soil moisture based on dynamic vegetation scattering properties for AMSR-E. *IEEE Transactions on Geoscience and Remote Sensing*, 1–12.

Entekhabi, D., Njoku, E. G., O'Neill, P. E., Kellogg, K. H., Crow, W. T., Edelstein, W. N., ... Van Zyl, J. (2010). The soil moisture active passive (SMAP) mission. *Proceedings of the IEEE, 98*(5), 704–716.

Hellkvist, J., Richards, G. P., & Jarvis, P. G. (1974). Vertical gradients of water potential and tissue water relations in sitka spruce trees measured with the pressure chamber. *Journal of Applied Ecology, 11*(2), 637.

Jackson, T. J., & Schmugge, T. J. (1991). Vegetation effects on the microwave emission of soils. *Remote Sensing of Environment, 36*(3), 203–212.

Jackson, T. J., Hsu, A. Y., & O'Neill, P. E. (2002). Surface soil moisture retrieval and mapping using high-frequency microwave satellite observations in the Southern Great Plains. *Journal of Hydrometeorology, 3*(6), 688–699.

Janott, M., Gayler, S., Gessler, A., Javaux, M., Klier, C., & Priesack, E. (2011). A one-dimensional model of water flow in soil–plant systems based on plant architecture. *Plant and Soil, 341*(1–2), 233–256.

Jones, M. O., Jones, L. A., Kimball, J. S., & McDonald, K. C. (2011). Satellite passive microwave remote sensing for monitoring global land surface phenology. *Remote Sensing of Environment, 115*(4), 1102–1114.

Kerr, Y., Waldteufel, P., Richaume, P., Davenport, L., Ferrazzoli, P., & Wigneron, J. -P. (2011). Algorithm theoretical based document (ATBD) for the SMOS level 2 processor for soil moisture. *Tech. Rep.* CESBIO, IPSL-Service dAronomie, INRA-EPHYSE, Reading University, Tor Vergata University.

Kerr, Y. H., Waldteufel, P., Richaume, P., Wigneron, J. -P., Ferrazzoli, P., Mahmoodi, A., ... Delwart, S. (2012). The SMOS soil moisture retrieval algorithm. *IEEE Transactions on Geoscience and Remote Sensing, 50*(5), 1384–1403.

Klein, L., & Swift, C. (1977). An improved model for the dielectric constant of sea water at microwave frequencies. *IEEE Transactions on Antennas and Propagation, 25*(1), 104–111.

Konings, A. G., Entekhabi, D., Chan, S. K., & Njoku, E. G. (2011). Effect of radiative transfer uncertainty on L-band radiometric soil moisture retrieval. *IEEE Transactions on Geoscience and Remote Sensing, 49*(7), 2686–2698.

Konings, A. G., McColl, K. A., Piles, M., & Entekhabi, D. (2015). How many parameters can be maximally estimated from a set of measurements? *IEEE Geoscience and Remote Sensing Letters, 12*(5), 1081–1085.

Kurum, M. (2013). Quantifying scattering albedo in microwave emission of vegetated terrain. *Remote Sensing of Environment, 129*(0), 66–74.

Kurum, M., O'Neill, P. E., Lang, R. H., Joseph, A. T., Cosh, M. H., & Jackson, T. J. (2012). Effective tree scattering and opacity at L-band. *Remote Sensing of Environment, 118*(0), 1–9.

Lawrence, H., Wigneron, J. -P., Richaume, P., Novello, N., Grant, J., Mialon, A., ... Kerr, Y. (2014). Comparison between SMOS vegetation optical depth products and MODIS vegetation indices over crop zones of the USA. *Remote Sensing of Environment, 140*(0), 396–406.

jul Le Vine, D. M., Lagerloef, G. S. E., Colomb, F. R., Yueh, S. H., & Pellerano, F. A. (2007). Aquarius: An instrument to monitor sea surface salinity from space. *IEEE Transactions on Geoscience and Remote Sensing, 45*(7), 2040–2050.

Le Vine, D. M., De Matthaeis, P., Ruf, C. S., & Chen, D. D. (2014). Aquarius RFI detection and mitigation algorithm: Assessment and examples. *IEEE Transactions on Geoscience and Remote Sensing, 52*(8), 4574–4584.

Liu, Y. Y., de Jeu, R. A. M., McCabe, M. F., Evans, J. P., & van Dijk, A. I. J. M. (2011). Global long-term passive microwave satellite-based retrievals of vegetation optical depth. *Geophysical Research Letters, 38*(18) (L18402–).

Liu, Y. Y., van Dijk, A. I. J. M., de Jeu, R. a. M., Canadell, J. G., McCabe, M. F., Evans, J. P., & Wang, G. (2015). Recent reversal in loss of global terrestrial biomass. *Nature Climate Change* (May).

McColl, K. A., Entekhabi, D., & Piles, M. (2014). Uncertainty analysis of soil moisture and vegetation indices using Aquarius scatterometer observations. *IEEE Transactions on Geoscience and Remote Sensing, 52*(7), 4259–4272.

Meesters, A., de Jeu, R. A. M., & Owe, M. (2005). Analytical derivation of the vegetation optical depth from the microwave polarization difference index. *IEEE Geoscience and Remote Sensing Letters, 2*(2), 121–123.

Mironov, V. L., Dobson, M. C., Kaupp, V. H., Komarov, S. A., & Kleshchenko, V. N. (2004). Generalized refractive mixing dielectric model for moist soils. *IEEE Transactions on Geoscience and Remote Sensing, 42*(4), 773–785.

O'Neill, P., Chan, S., Njoku, E., Jackson, T., & Bindlish, R. (2012). Algorithm theoretical basis document SMAP level 2 & 3 soil moisture (passive). *Tech. Rep. Jet Propulsion Laboratory, California Institute of Technology, Initial Release, Vol. 1*, .

Owe, M., de Jeu, R., & Walker, J. (2001). A methodology for surface soil moisture and vegetation optical depth retrieval using the microwave polarization difference index. *IEEE Transactions on Geoscience and Remote Sensing, 39*(8), 1643–1654.

Owe, M., de Jeu, R., & Holmes, T. (2008). Multisensor historical climatology of satellite-derived global land surface moisture. *Journal of Geophysical Research - Earth Surface, 113*(F1).

Patton, J., & Hornbuckle, B. (2013). Initial validation of SMOS vegetation optical thickness in Iowa. *IEEE Geoscience and Remote Sensing Letters, 10*(4), 647–651.

Piles, M., Vall-llossera, M., Camps, A., Talone, M., & Monerris, A. (2010). Analysis of a least-squares soil moisture retrieval algorithm from L-band passive observations. *Remote Sensing, 2*(1), 352–374.

Piles, M., McColl, K. A., Entekhabi, D., Das, N., & Pablos, M. (2015). Sensitivity of Aquarius active and passive measurements temporal covariability to land surface characteristics. *IEEE Transactions on Geoscience and Remote Sensing, 53*(8), 4700–4711.

Poulter, B., Frank, D., Ciais, P., Myneni, R. B., Andela, N., Bi, J., ... van der Werf, G. R. (2014). Contribution of semi-arid ecosystems to interannual variability of the global carbon cycle. *Nature, 509*(7502), 600–603.

Rahmoune, R., Ferrazzoli, P., Kerr, Y. H., & Richaume, P. (2013). SMOS level 2 retrieval algorithm over forests: Description and generation of global maps. *IEEE Journal of Selected Topics in Applied Earth Observations and Remote Sensing, 6*(3), 1430–1439.

Reichle, R. H., & Liu, Q. (2014). *Observation-corrected precipitation estimates in GEOS-5. NASA/TM2014-104606, Vol. 35*, .

jul Reichle, R. H., Koster, R. D., De Lannoy, G. J. M., Forman, B. A., Liu, Q., Mahanama, S. P. P., & Touré, A. (2011). Assessment and enhancement of MERRA Land surface hydrology estimates. *Journal of Climate, 24*(24), 6322–6338.

dec Schimel, D., Stephens, B. B., & Fisher, J. B. (2014). Effect of increasing CO_2 on the terrestrial carbon cycle. *Proceedings of the National Academy of Sciences, 112*(2), 436–441.

jun Schlesinger, W. H., & Jasechko, S. (2014). Transpiration in the global water cycle. *Agricultural and Forest Meteorology, 189–190*, 115–117.

Shi, J., Jackson, T., Tao, J., Du, J., Bindlish, R., Lu, L., & Chen, K. S. (2008). Microwave vegetation indices for short vegetation covers from satellite passive microwave sensor AMSR-E. *Remote Sensing of Environment, 112*(12), 4285–4300.

Simpson, E. H. (1949). Measurement of diversity. *Nature*, 688.

Ulaby, F. T., & Long, D. G. (2014). *Microwave radar and radiometric remote sensing.* Ann Arbor: University of Michigan Press.

Ulaby, F. T., Moore, R. K., & Fung, a. K. (1986). From theory to applications. *Vol. III of Microwave remote sensing: Active and passive.* Norwood, MA: Artech House.

Van de Griend, A. A., & Owe, M. (1994). Microwave vegetation optical depth and inverse modeling of soil emissivity using Nimbus SMMR satellite-observations. *Meteorology and Atmospheric Physics, 54*(1–4), 225–239.

Van De Griend, A. A., & Wigneron, J. -P. (2004). The b-factor as a function of frequency and canopy type at H-polarization. *IEEE Transactions on Geoscience and Remote Sensing, 42*(4), 786–794.

Van der Schalie, R., Parinussa, R., Renzullo, L., van Dijk, A., Su, C. -H., & de Jeu, R. (2015). SMOS soil moisture retrievals using the land parameter retrieval model: Evaluation over the Murrumbidgee Catchment, southeast Australia. *Remote Sensing of Environment, 163*, 70–79.

Van der Schalie, R., Kerr, Y., Wigneron, J., Rodrguez-Fernández, N., Al-Yaari, A., & Jeu, R. (2015). Global SMOS soil moisture retrievals from the land parameter retrieval model. *International Journal of Applied Earth Observation and Geoinformation* http://dx.doi.org/10.1016/j.jag.2015.08.005 (in press).

Van Emmerik, T., Steele-Dunne, S. C., Judge, J., & van de Giesen, N. (2014). Impact of diurnal variation in vegetation water content on radar backscatter of maize during water stress. *IEEE Transactions on Geoscience and Remote Sensing, 16*(7), 6070.

Van Zyl, J., & Kim, Y. (2011). Synthetic aperture radar polarimetry. *JPL space science and technology series.* Hoboken, NJ: Wiley.

Wigneron, J. P., Waldteufel, P., Chanzy, a., Calvet, J. C., & Kerr, Y. (2000). Two-dimensional microwave interferometer retrieval capabilities over land surfaces (SMOS mission). *Remote Sensing of Environment, 73*(3), 270–282.

Wigneron, J. -P., Parde, M., Waldteufel, P., Chanzy, A., Kerr, Y., Schmidl, S., & Skou, N. (2004). Characterizing the dependence of vegetation model parameters on crop structure, incidence angle, and polarization at L-band. *IEEE Transactions on Geoscience and Remote Sensing, 42*, 416–425.

Zhou, L., Tian, Y., Myneni, R. B., Ciais, P., Saatchi, S., Liu, Y. Y., ... Hwang, T. (2014). Widespread decline of Congo rainforest greenness in the past decade. *Nature, 509*(7498), 86–90.